Draft 4/7/2014

The mobility of Nb in rutile-saturated NaCl- and NaF-bearing aqueous fluids from 1-6.5 GPa and 300-800°C

ELIZABETH A. TANIS[1,2], ADAM SIMON[1], OLIVER TSCHAUNER[2,3] PAUL CHOW[4], YUMING XIAO[4], PAMELA BURNLEY[2,3], CHRIS CLINE[3], JOHN M. HANCHAR[5], THOMAS PETTKE[6], GUOYIN SHEN[5], YUSHENG ZHAO[5]

[1]Earth & Environmental Sciences, University of Michigan
[2]HiPSEC, University of Nevada, Las Vegas
[3]Department of Geoscience, University of Nevada, Las Vegas
[4]HPCAT, Carnegie Institute of Washington, Argonne IL
[5]Earth Sciences, Memorial University of Newfoundland
[6]Institute of Geological Sciences, Bern, Switzerland

ABSTRACT

Rutile (TiO_2) is an important host for high field strength elements (HFSE) such as Nb in metamorphic and subduction zone environments. The observed depletion of Nb in arc rocks is often explained by the hypothesis that rutile sequesters HFSE in the subducted slab and overlying sediments, and is chemically inert with respect to aqueous fluids evolved during prograde metamorphism in the forearc to subarc environment. However, field observations in exhumed terranes, and experimental studies indicate that HFSE may be soluble in complex aqueous fluids at high pressure (i.e., > 0.5 GPa) and moderate to high temperature (i.e., > 300°C). In this study, we investigated experimentally the mobility of Nb in NaCl- and NaF-bearing aqueous fluids in equilibrium with Nb-bearing rutile at pressure-temperature conditions applicable to fluid evolution in arc environments. Niobium concentrations in aqueous fluid were measured directly by using a hydrothermal diamond anvil cell (HDAC) as the sample container and synchrotron x-ray fluorescence (SXRF) at 2.1 to 6.5 GPa and 300-500°C (HDAC), and indirectly by performing mass loss experiments in a piston-cylinder (PC) apparatus at ~1 GPa and 687-793°C. The Nb concentration in a 10 wt% NaCl aqueous fluid increases from 7 to 153 ppm as temperature increases from 300 to 500°C, over a pressure range from 2.1 to 2.8 GPa, consistent with a positive temperature dependence. The concentration of Nb in a 20 wt% NaCl aqueous fluid varies from 74 to 233 ppm at 300 to 500°C, over a pressure range from 1.8 to 6.4

GPa; however, there is no discernable temperature or pressure dependence. The Nb concentration in a 4 wt% NaF-bearing aqueous fluid increases from 223 to 1,339 ppm as temperature increases from 300 to 500°C over the pressure range 2.1 to 6.5 GPa. The concentration of Nb in a 4 wt% NaF-bearing fluid at 692°C and 1 GPa is 223 ppm. The data for the F-bearing fluid indicate that the Nb content of the fluid exhibits a temperature dependence between 300 and 500°C at ≥2 GPa, but there is no observed dependence on pressure. Together, the data demonstrate that the hydrothermal mobility of Nb is strongly controlled by the composition of the fluid, consistent with published data for Ti. At all experimental conditions, however, the concentration of Nb in the fluid is always lower than coexisting rutile, consistent with a role for rutile in moderating the Nb budget of arc rocks.

INTRODUCTION

Arc magmas bear a characteristic geochemical trace element signature consisting of a depletion of high field strength elements (HFSE) and enrichment in large ion lithophile elements (LILE) and light rare earth elements (LREE) relative to mid-ocean ridge basalts (Gill, 1981; Hawkesworth et al., 1991). Three working hypotheses have been developed to explain the geochemical signature of arc magmas. The *first* hypothesis is that ascending aqueous fluids from the slab are enriched in LILE and LREE, relative to HFSE, and thus transfer this signature to partial melts produced in the mantle. This hypothesis suggests that mineral phases (e.g., clinopyroxene) in the mantle control the HFSE budget of mantle-derived silicate melt (Hawkesworth, 1993a,b; Kelemen et al., 1990; Foley et al., 2000, Audétat and Keppler, 2005). The *second* hypothesis is that melt extraction from the mantle at a back-arc spreading center depletes the mantle in HFSE prior to its interaction with slab-derived fluid at the base of the arc volcano plumbing system (McCulloch and Gamble, 1991; Woodhead et al., 1993). This

hypothesis requires the mantle wedge to be re-fertilized by fluids during melt extraction. The downward motion of the subducted slab drags this depleted mantle material into the mantle wedge above the slab, yielding a strong depletion of HFSE during subsequent partial melting of the depleted mantle.

The *third* and most widely accepted hypothesis is that rutile in the subducted slab retains the HFSE during slab dehydration; hence, rutile moderates the HFSE chemistry of fluids that ascend into the mantle (Saunders et al., 1980; Green, 1981; Brophy and Marsh, 1986; Ryerson and Watson, 1987; Morris et al., 1990). The resulting trace element abundance patterns are preserved in arc magma owing to the very low abundances of the HFSE in the mantle and slab-evolved fluid. Experimental studies of rutile solubility in pure H_2O support this hypothesis (Audétat and Keppler, 2005; Tropper and Manning, 2005). However, Manning (2004) emphasized that slab-derived fluids are not pure H_2O, but rather contain significant amounts (i.e., up to and exceeding 10 wt% dissolved solutes) of alkalis (Na, K), halogens (Cl, F) and aluminosilicate components (i.e., Si, Al). Experimental data generated at 0.5-2 GPa and 700-1100°C demonstrate that the addition of these solutes to aqueous fluid increases the solubility of pure rutile in the fluid by several orders of magnitude relative to pure water (Audétat and Keppler, 2005; Antignano and Manning, 2008; Manning et al., 2008; Rapp et al., 2010; Hayden and Manning, 2011). For example, at 800°C and 1 GPa, the solubility of pure rutile in aqueous fluid increases from 18 ± 5 ppm Ti in pure water to 152 ± 5 ppm Ti in aqueous fluid that contains 3.162 – 2.423 wt% dissolved silicate (Antignano and Manning, 2008). Rapp et al. (2010) reported that at 800°C and 0.5 GPa, the solubility of pure rutile in aqueous fluid increased from 212 ± 18 ppm Ti in pure water to 11,912 ppm Ti in fluid that contains 10 wt% dissolved NaF. These experimental data evince that the solubility of pure rutile in aqueous fluid varies with fluid chemistry. However,

existing experimental data do not overlap with the pressure-temperature paths for subduction zones (Figure 1; Hacker, 2008) and require extrapolation when applied to the conditions of fluid evolution during prograde metamorphic devolatilization, which begins in the forearc at temperatures as low as 300°C (cf. Bebout et al., 1999; Hacker, 2008). Notably, all of the aforementioned studies used the solubility of pure rutile in aqueous fluid as a proxy to predict the fluid mobility of all HFSE. It has been shown that this may be appropriate for Zr (Kelemen et al., 1990). However, Jenner et al. (1994) reported much higher rutile / tonalite melt partition coefficients for Nb ($D_{Nb}^{rutile/fluid} = 52.6$) and Ta ($D_{Ta}^{rutile/fluid} = 99.5$) then for Zr ($D_{Zr}^{rutile/fluid} = 4.76$), indicating the potential error of inferring the mobility of Nb and Ta based on Ti.

The enhanced fluid compatibility of Ti in complex aqueous solutions suggests that Nb may be soluble in such fluids. There are an absence of data that constrain the mobility of HFSE such as Nb in aqueous fluid. Brenan et al., (1994) and Stalder et al. (1998) experimentally investigated the partitioning of Nb between rutile and aqueous fluid at 1-5 GPa and 900-1100 °C. These pressures overlap with those in the forearc to subarc, but the temperatures are higher by several hundred degrees then those obtained by subduction (Figure 1). The experimenal assemblage of Stalder et al. (1998) contained only pure H_2O, whereas Brenan et al. (1994) added 3 wt% SiO_2 in addition to HCl, NaCl and Al separately to the fluid in three experiments. Brenan et al. (1994) reported that the addition of NaCl, HCl and Al to the fluid-rutile assemblage affected the value $D_{Nb}^{fluid/rutile}$. For example, at 900°C and 1 GPa, the value of $D_{Nb}^{fluid/rutile}$ (± 1σ) was 237 ± 43 for water with 3 wt% SiO_2, and increased to 9100 ± 3100 with the addition of 1*m* HCl-fluid, 10,940 ± 3610 with the addition of 1*m* NaCl-fluid, and 13,000 ± 3770 for fluid that contained 300 ppm Al. Similar results were reported for Ta (Brenan et al., 1994). These results suggest that the mobility of HFSE in equilibrium with rutile is quite low and that the partitioning of HFSE from

rutile to aqueous fluid actually decreases with increasing complexity of the aqueous fluid. This finding disagrees with data for pure rutile as mentioned above.

To quantitatively evaluate the fluid mobility of HFSE in light of the more recent experimental studies mentioned above that support a strong role of fluid chemistry in dissolving rutile (up to 1 wt% Ti in the fluid), and presumably other HFSE, there is the critical need to assess experimentally the effects of prograde metamorphic devolatilization and the relationship between fluid chemistry and trace element mobility at pressures and temperatures where fluids evolve during subduction (Figure 1). In this study, new experimental data is presented that quantify the mobility of Nb in rutile-saturated NaCl- and NaF-bearing aqueous fluids at 1 to 6.5 GPa and temperatures of 300 to 800°C, conditions appropriate for prograde devolatilization paths in cold to hot subduction zones.

EXPERIMENTAL METHODS

Rutile Synthesis and Characterization

The synthetic Nb-doped rutile (Nb-TiO_2) crystals used in this study were prepared following the method described in Hanchar et al. (2001). High-purity TiO_2 and Nb_2O_5 were weighed to achieve 6 mol% TiO_2 and 0.09 mol% Nb_2O_5, then mixed in an HNO_3-cleaned agate mortar and pestle under absolute ethanol and allowed to dry. Once dried, the powders were mixed under absolute ethanol with the fluxing agents Li_2MoO_4 and MoO_3 in the following proportions: 84 mol% MoO_3 and 10 mol% Li_2MoO_4; and the remaining TiO_2 - Nb_2O_5 mixture, mentioned above, then allowed to dry. The mixture was then transferred to a clean Pt crucible with a tightly fitted Pt lid. The crucible was lowered into the “hottest spot” of a preheated (1200°C) Deltech $MoSi_2$ vertical tube furnace and held at constant temperature for seven days, permitting the flux to evaporate. Using a type S control thermocouple, the temperature in the hot spot was measured to

123 be stable within 5 C. When rutile saturation was reached, the rutile crystals began to grow in
124 the residual flux. Upon completion of the synthesis, no residual flux remained in the crucible.
125 The crystals were removed from the Pt crucible with tweezers and cleaned in concentrated
126 HNO_3. Powder x-ray diffraction was performed to ensure that the rutile structure was obtained
127 and not the TiO_2 polymorphs brookite or anatase.
128 The concentrations of Nb, Ti and Mo in the starting rutile were quantified by using
129 wavelength dispersive spectroscopy on a Cameca SX100 electron probe microanalyzer (EPMA)
130 and laser ablation inductively coupled mass spectroscopy (LA-ICP-MS). For EMPA, a beam
131 current of 50 nA (calibration and analysis) and an accelerating voltage of 15 kV were used.
132 Collimators were used to reduce peak interferences and to maximize peak-to-background ratios.
133 Counting times (30 s at the Nb and Ti peak) yielded detection limits for Nb, Ti, and Mo of
134 approximately 328, 590 and 300 ppm, respectively. Standard ZAF techniques were used for the
135 matrix corrections. The standards used included pure rutile, Nb_2O_5 and pure Mo metal. A
136 different crystal and detector combination was used for each element: LIF for Ti and LPET for
137 Nb and Mo. Each crystal was imaged by using back scattered electrons (BSE), and an EMPA
138 line traverse across the length of the sample was performed to evaluate chemical homogeneity.
139 The concentrations of Nb and Mo of starting crystals were 0.95 ± 0.1 wt%, and 0.02 ± 0.03 wt%,
140 respectively; Mo is sourced form the flux used during mineral synthesis. Some crystals
141 displayed zoning in BSE images, and for these crystals an analytical line traverse from the rim to
142 the core of the crystal was preformed by using a 5 μm beam size and a center to center distance
143 of 2 μm for each spot analysis (Figure 2 a, b, c). All totals summed to 100 ± 1%. Depth profiles
144 of the Nb concentration through starting and run-product rutile crystals were also obtained by
145 using LA-ICP-MS. The LA-ICP-MS analyses were performed following the principles outlined

in Pettke (2006**).** Depth profiling was performed by single pulse analyses where each pulse corresponded to 0.10 mm depth. The data indicate that the starting crystals contain 1.03 ± 0.2 wt% Nb, which is consistent with the EMPA results. The LA-ICP-MS data also indicate that some starting crystals have a narrow rim that is enriched in Nb and Mo (Figures 2 d, e and 3a). For example, the LA-ICP-MS depth profile shown in Figure 2e indicates that the concentration of Nb at the rim of this starting rutile crystal was ~8 wt. %, and decreased to ~1 wt. % over a distance of 9 microns into the center of the crystal. This Nb-enriched rim likely reflects either a quench-effect during synthesis, or the kinetics of Nb incorporation into rutile during synthesis. We emphasize that all run-product crystals were homogeneous with respect to Nb and Ti, and contained no detectable Mo, which we interpret to reflect the attainment of chemical equilibrium with the fluid at run conditions, as discussed below.

SXRF experiments

The HDAC (Bassett et al., 1993) used in the current study was equipped with two opposing 500 or 800 μm culet diamonds. Molybdenum wires, coiled around a tungsten carbide seat that supported each diamond anvil, provided resistive heating. Two K-type (NiCr-NiAl) thermocouples, one on each diamond, were used to measure temperature. The HDAC was heated resistively by using variable transformers that facilitated flexible heating rates and allowed us to maintain temperature to 5°C. The HDAC was calibrated up to 800 C by observing the melting point or phase transition of $NaNO_3$, CsCl, and NaCl, and measured temperatures were systematically lower by ~0.85% over the entire range studied (Kerrigan, 2011). A 1% H_2-Ar gas mixture flowed constantly through the HDAC during the measurements to prevent corrosion of the diamonds and the heaters.

A gold-lined rhenium gasket was pre-indented to a thickness of ~120 μm and a hole of

200 μm or 400 μm diameterwas drilled for 500 and 800 μm culets, respectively. A Nb-rutile crystal, measuring approximately 40x40x20 μm by using a optical microscope, was loaded into the sample chamber. Deionized H_2O containing either 10 wt% NaCl, 20 wt% NaCl or 4 wt% NaF, was then added by using a micro syringe and the HDAC was immediately sealed and pressurized to 0.5 GPa.

The SXRF experiments were performed at undulator beamline 16-IDD (HPCAT) at the Advanced Photon Source (APS) synchrotron facility at Argonne National Laboratory. The incident beam energy was 27 keV. The beam was focused to a spot size of 35x50 μm full-width at half maximum (FWHM) by using a pair of Kirkpatrick-Baez mirrors. A 100 μm round pinhole was used before the HDAC to reduce the tails of the incident beam, which contained a flux of 1.14 10^{12} photons/s/mm^2. The incident beam was projected into the sample chamber through the diamonds of the HDAC. The fluorescence from the sample was collected in a 170° backscattering geometry by using a Vortex-EX silicon drift detector that was positioned ~0.8 meters from the sample. To reduce the background, a pair of large collimating slits was placed before the detector. The energy channels of the multi-channel analyzer were calibrated with ^{55}Fe, ^{57}Co, and ^{109}Cd radioactive sources. The position and aperture of the detector was optimized by using the SXRF peak of pure Nb metal. There is no Nb contamination from any component of the HDAC, which was confirmed by SXRF analyses of an empty cell.

The Nb-rutile crystal position was found visually by using an online optical microscope and confirmed by SXRF. The beam was then positioned ≥50 μm away from the crystal and the HDAC was rotated 5° to ensure no signal contamination from the crystal. The HDAC was heated at experimental pressure to 300 °C, and pressure was monitored throughout the run by collecting XRD patterns of Au from a MAR 165 CCD detector placed in the forward scattering direction.

The XRD patterns were integrated and corrected for geometric distortions by using Fit2D (Hammersley, 1997). A NIST standard CeO_2 pattern was collected and used for the XRD calibration. Gold pressure was determined by using the method of Dorogokupets and Dewaele (2007). Fluorescence spectra for Nb were collected iteratively in 300 s intervals. We assessed equilibrium by evaluating the time-dependence of the fluorescence signal. Once the Nb peak area, at a unique pressure and temperature condition, became time-invariant, it was interpreted to reflect the attainment of steady-state conditions and proximity to chemical equilibrium. This took approximately 30–40 minutes at each unique pressure-temperature point. The time to reach steady state is consistent with observations reported by Manning et al. (2008), Schmidt et al. (2007), and Sanchez-Valle et al. (2003). Once steady-state conditions were achieved, spectra were collected in 300 s intervals for ~3 h. The temperature was then increased to 400°C, and subsequently to 500°C, and the data collection procedure was repeated at each temperature. The experimental run conditions and results are reported in Table 1. During heating and cooling, there is some relaxation of the HDAC. This can cause deformation in the gasket sample chamber and result in a slight change in pressure. This change was observed and therefore pressure was measured before and after each sequence of fluorescence data collected. The fluorescence spectra from the standard solutions and high P-T experiments were separately summed, and normalized to transmitted beam flux and time. A linear background was subtracted and the area of the Nb fluorescence peak was fit and integrated by using Fityk (Wojdyr, 2010). Uncertainties for the Nb concentration of the fluids measured in the SXRF experiments were calculated based on the fitting errors of the summed spectra, and also include propagating the fitting errors from the standard calibration to determine Nb concentrations at high pressure and temperature. Due to the iterative nature of the SXRF experimental technique, recovering and analyzing the rutile

crystal from each unique pressure-temperature condition is not possible. Thus, partition coefficients for Nb between fluid and rutile were not measured. The concentration of Nb in aqueous fluid that was equilibrated with rutile was measured and the results reported here.

SXRF Mapping

A new data collection method was employed for experimental run 2013_02_05 (300-600^{o} C, 2.13-3.07 GPa). The cell was positioned in direct line of the detector (versus angled to hide the crystal signal) to maximize Nb count rate. The position of the HDAC was moved in steps of 25 μm in the x and y directions and XRF spectra were taken at each x-y position, as well as, the values of the incoming and out going beam intensity. Figures 4a and b demonstrates how the sample chamber was mapped in 2-D (x and y position, where the color scale is beam intensity) and in 3-D (x and y position and z axis as well as color scale is the intensity), respectively. Figures 4c and d are similar 2-D and 3-D figures that show how the spatial position of the Nb-rutile crystal is constrained. The concentration of Nb in the fluid was determined by summing and integrating the normalized spectra, significantly away (50-75 μm) from the Nb-rutile crystal spectra. A map of the HDAC containing 300 and 600 ppm Nb standard were also collected for calibration.

Piston Cylinder Mass Loss Experiments

The mass loss experiments were conducted in a Griggs-type modified piston-cylinder apparatus. Run conditions are provided in Table 2. Temperature gradients were modeled by using the "CellAssembly" thermal modeling program (Hernlund et al., 2006), and confirmed by using two thermocouples placed on each side of the capsule. The temperature gradient was a maximum of 5°C across all dimensions (~7 mm long, 5 mm in diameter) of the capsule. Confining pressure on the sample was derived from the oil pressure in the piston cylinder ram,

238 which was measured with an Omegadyne pressure transducer. The nominal sample pressure was
239 calculated by dividing the load exerted by the ram by the area of the confining pressure piston.
240 The nominal sample pressure can deviate from the actual pressure by up to 10% owing to
241 frictional effects (Bose and Ganguly, 1995; Burnley and Getting, 2012). The experimental
242 charges contained a single crystal of Nb-rutile and 30 μg fluid in a 5 mm OD platinum capsule.
243 The capsule design was made by cutting a ~7 mm length piece of Pt tubing and welding a
244 circular disk "lid" onto the bottom and top (after it was loaded). The starting crystal was weighed
245 four times by using a Mettler XP26 DeltaRange balance, and the valued averaged for accuracy,
246 before being loaded into the capsule. The hot piston-in technique of Manning and Boettcher
247 (1994) was used to cold compress to ~ 50 MPa and then heating and compressing in alternating
248 increments to minimize compression and expansion of the capsule relative to other sample
249 assembly parts. Conditions were maintained for ≥8 hours once the desired pressure and
250 temperature were attained. The sample was quenched by shutting off power to the apparatus,
251 which results in a temperature drop of <30°C in <30 s. This minimizes, if not eliminates, back-
252 reaction between the crystal and fluid during quench (Antignano and Manning, 2008). After
253 quench, the capsule was cleaned and weighed, then punctured and dried at 120°C for 1 hour. The
254 capsule was weighed again, opened, and the crystal was removed. Comparison of the total
255 capsule weight before and after the experiments showed no fluid was lost during the experiment.
256 The crystal was cleaned with isopropanol and weighed 4 times to determine the average mass
257 loss.
258 Piston cylinder run products included the partially dissolved starting crystal and fine-
259 grained quench "roe" crystals (run 20130522), consistent with crystals that formed during
260 quench (cf. Antignano and Manning, 2008). In experiment 20130527, broken crystal fragments

were recovered along with the primary crystal. Final concentrations of Nb and Mo of rutile crystals recovered from the mass-loss experiments were determined by using EMPA and LA-ICP-MS, as previously described. The EMPA and LA-ICP-MS results demonstrate that run-product crystals were homogeneous with respect to Nb and Ti, and contained no detectable Mo. Uncertainties for Nb concentrations in the fluid from the mass loss experiments reflect propagation of weighing errors, the analytical error from the EMPA and LA-ICP-MS analysis, as well as consideration of a *possible* Nb-enriched rim on the starting rutile crystal. To include the error of the starting crystal containing a Nb-enriched rim, a minimum value of mass loss was calculated by using the final (bulk) Nb concentration of the recovered rutile crystal from each experiment, determined by using EMPA and LA-ICP-MS, and a maximum value assuming only the Nb-enriched rim (5 wt%) was dissolved. For example, in experiment 20130314 the mass loss is 24 μg, if a spherical crystal is assumed this corresponds to a radius difference of ~5 μm, which is on the order of the rim distance for some of the starting crystals. Therefore it can be assumed that if the crystal is homogeneous the amount of Nb going into the fluid based on the final composition (0.9 wt%) is 11ppm, however *if* it contained a 5 wt% rim then the concentration would be 59 ppm.

RESULTS

The concentration data for Nb in a 10 wt% NaCl – H_2O fluid, 20 wt% NaCl – H_2O fluid, and 4 wt% NaF – H_2O fluid are provided in Tables 1 (HDAC) and 2 (piston-cylinder), respectively. Niobium concentrations in the fluid as a function of a) temperature, b) pressure and c) density are presented in Figure 5. Lines in Figure 5 are illustrative only and are not statistical best fits. The density of the aqueous fluid at run conditions was calculated by using the equation of state (EOS) for pure H_2O (Abramson and Brown, 2004), and, in the case of NaCl-H_2O fluids,

the EOS from Mantegazzi (2013). There is no published EOS for NaF-bearing aqueous fluid; hence, the density of pure water was used for reference. Niobium concentrations in 10 wt% NaCl-bearing aqueous fluid at 2.1-2.8 GPa range from 7.3 ppm at 300°C to 13.4 ppm at 500°C (Table 1; Figure 5), and at 1 GPa from 11 ppm at 687°C to 79 ppm at 793°C (Table 2; Figure 5a). The data indicate positive temperature dependence for the concentration of Nb in the 10 wt% NaCl-bearing aqueous fluid, and a negative pressure and density dependence (Figure 5). The concentration of Nb in a 20 wt% NaCl-bearing aqueous fluid over the temperature range 300 to 600°C varies from 74 to 233 ppm, which is an increase of 2 to 3 times that of the 10 wt% NaCl-bearing fluid. However, there is no temperature, pressure and density dependance observed for the 20 wt% NaCl-bearing aqueous fluid. The Nb concentration of the 4 wt% NaF-bearing fluid ranges from 272 ppm at 300°C and 2.13 GPa to 1,339 ppm at 500°C and 3.07 GPa, and decreases to 223 ppm at 692°C and 1 GPa. Thus, the addition of NaF to the aqueous fluid, relative to NaCl, increases by 1 to 2 orders of magnitude the concentration of Nb in the fluid. The concentration of Nb in the 4 wt% NaF-bearing fluid exhibits a positive temperature dependence between 300 and 500°C at >2 GPa, and no pressure or density dependence. Overall, the new data presented here indicate that concentration of Nb in saline fluids is strongly dependent on the nature and concentration of the predominant anion (i.e., Cl *vs*. F) of the fluid.

Comparison to Published Data

In Figure 5, the experimentally determined Nb concentrations of rutile-saturated aqueous fluids from two published studies are plotted for comparison with data from the current study. Figure 5 aq showsw the dependence of Nb concentration as function of temperature. Figure 5 b shows…. 5 c shows.

While in our experiments Nb-bearing rutile was reacted with NaCl- and NaF-bearing aqueous fluids of different degrees of salinity: Our 10wt% data exhibit a lesser T dependence than the pure H2O- and the Stalder et al. (1998) equilibrated a solid assemblage of clinopyroxene and rutile with pure H_2O at 5 GPa and 1000°C; the clinopyroxene/rutile ratio was 9:1 and 1:1 in the two experiments. They reported that the fluid contained 10.9 ppm and 37.6 ppm in the two assemblages, respectively, and that the value of $D_{Nb}^{rutile/melt}$ decreased from 0.12 to 0.05, respectively. Brenan et al. (1994) equilibrated rutile and aqueous fluid at 1 and 2 GPa and 900 and 1100°C. The experimenal fluids in the study of Brenan et al. (1994) contained ~3 wt% dissolved SiO_2, and varied from pure SiO_2-bearing H_2O, to 1*m* HCl-bearing H_2O, to 1*m* NaCl-bearing H_2O, and one experiment with ~300 ppm dissolved Al. Their data indicate that the concentration of Nb in the fluid phase varies by one order of magnitude, from ~ 20 to 300 ppm, for pure H_2O, and was ~30 ppm for a 5.8 wt% NaCl-bearing fluid.

Formatted: Highlight

The data for pure H_2O from Brenan et al. (1994) and Stalder et al. (1998) indicate that the concentration of Nb in rutile-saturated H_2O exhibits a positive temperature dependence over the range 900 to 1100°C. This is consistent with the new data presented here for the concentration of Nb in a 10 wt% NaCl- and 4 wt% NaF-bearing aqueous fluid (Figure 5a). Our data indicate that Nb-solubility in aqueous fluid increases markedly with the salinity. In addition, fluoride induces a stronger increase in solubioity than Cl. We note that the temperature dependence of the solubility in salinic fluids decreases with increasing solubility. This can be ssen when comparing the data for pure H2O (Stld,Brnan) and xxx % HCl (Brenan) to our data with 10wt% NaCl. Moreover, our set of data for fluid with 20wt% NaCl do not exhibit any pressure dependence. We also note that the Nb si9olubuiity increases less with T for NaF- bearing fluid while the overall solubiity is an order of magnitude higher. These observations can be ratiobnalized based

on the strength of the Nb-Cl- and Nb-F- complexes which appear not be much affected by T while the amount of Cl and F available controls the solubility stronger than T.

An important implication of our data is that salinity is the dominant factor in Nb solubility while silicate- and aluminate activity have a comparatively much smaller effect. This finding is consistent with Rapp's observation ….

The data from Brenan et al. (1994) for the concentration of Nb in pure H_2O also indicate that the concentration of Nb in the fluid ~~exhibits a negative dependence~~decreases with pressure (Figure 5b) and fluid density (Figure 5c). This is consistent with ~~new~~ our results presented here for the concentration of Nb in a 10 wt% NaCl-bearing aqueous fluid. This suggest that the stability of the Nb-Cl complex(es) in the fluid decreases with pressure – either in total or by replacement of the complex dominant at low pressure by a different one at high pressure, which is less strongly binding Nb. We note that both our data for NaF-bearing and for the 20wt% Nacl -bearing fluid do not exhibit any pressure dependence. This can be rationalized as a pressure-invariant stability of the Nb-halogenide complexes. However, it does also imply that these compelxes are different than those dominant in the 10-wt% AnCl beatring fluid. The absence of a temperature dependence of Nb-solubility for the 2-wt% fluid and the weak dependence of the solubility on the NaF-bearing fluid are consistent with this. However, we cannot preclude the possibility of precipitation of Nb-bearing solids from the high-salinity fluids along with increasing T and changing P. Such precipitates may notbe captured in our experiments if they are concentrated along the gasket wall.

DISCUSSION

The new experimental data presented here demonstrate that at temperatures of 300 to 800°C and pressures ≥1 GPa, the addition of NaCl and NaF to rutile-saturated aqueous fluid

increases the concentration of Nb in the fluid to values higher than predicted from down-temperature extrapolations of experimental data for pure H_2O (Figure 5a). These new results for Nb are consistent with Rapp et al. (2010), who reported that the solubility of pure rutile in aqueous fluid, at 800-1000°C and 0.5 GPa, increased by approximately two orders of magnitude in aqueous fluid that contained 10 wt% NaCl and 10 wt% NaF, relative to pure H_2O. The new data suggest that Nb is complexed as Nb-chloride and Nb-fluoride in the NaCl-bearing and NaF-bearing experimental fluids, respectively. The determination that NaF enhances the concentration of Nb in aqueous fluid is consistent with predictions based on hard acid – soft base (HASB) considerations (Pearson, 1963), and observations from natural systems that Nb is hydrothermally transported during the evolution of ore deposits associated with alkaline magmatic systems (i.e., carbonatites; Singer, 1986; Verplanck and Van Gosen, 2011).

Timofeev et al. (2014) measured experimentally the solubility of Nb-oxide in F-bearing aqueous fluids at temperatures of 150 to 250°C and saturated water vapor pressure (SWVP). The activity of fluoride (a(F)), and pH were varied from ~10^{5} to 10^{-2} mF and 2.1 to 2.4., respectively. They reported that at low a(F) the concentration of Nb in the fluid was pH dependent, interpreted to indicate that Nb-fluoride complexes are present in the fluid. The concentration of Nb in the fluid increased with increasing a(F), independent of pH, which was interpreted to indicate that Nb in the fluid was present as a hydroxyfluoride complex. The relative strength of Nb-halide complexes was assessed computationally by Siegbahn (1993) who performed ab initio calculations to constrain the binding energies of Nb-halide complexes. Siegbahn (1993) reported that the binding energy of Nb-F (135 kcal/mol; bond distance of 1.97Å) is greater than Nb-Cl (101 kcal/mol; bond distance of 2.46Å), which is consistent with the the measured increase of Nb in the F-bearing aqueous fluid relative to the Cl-bearing aqueous fluid in the present study. In

general, binding energies for metal-halide complexes increase in the order Y > Zr > Mo > Tc > Ru > Rh > Pd, which is also consistent with findings for the strongly enhanced concentration of Y in Cl-bearing aqueous fluids at pressure-temperature conditions similar to those in the present study (Tanis et al., 2012). Siegbahn (1993) found that the increased strength of Nb-F relative to Nb-Cl is related to the interaction between the $4d_{\pi}$ orbital and the lone pairs of halides, which yields a symmetry that is conducive to attraction by electron donation. The consistency among experimental data sets reported by Timofeev et al. (2014) and Rapp et al. (2010), as well as the ab initio results reported by Siegbahn (1993), with the new data presented in this study seems to convincingly demonstrate that Nb is fluid-mobile as a Nb-halide complex in saline aqueous fluids.

The new data presented in this study have implications for the mobility of Nb in aqueous fluids evolved during prograde metamorphic dehydration reactions that occur during the subduction. Brouwer et al. (2012) reported an order of magnitude variation in the concentration of Nb in eclogites from the Franciscan Complex (California) and the Monviso Complex (Western Alps Lago Superiore region). These exhumed terranes equilibrated at a pressure of 1.05 GPa and 600 and 500^{o}C, respectively. Brouwer et al. (2012) invoked the composition of the fluid and degree of fluid-rock interaction as the cause of the order-of-magnitude variation in meaured Nb concentrations of the residual rock. The new data presented here indicate that only moderately saline aqueous fluid could effect the variability observed in the Franciscan and Monviso Complexes.

Gao et al. (2007) reported the presence of rutile crystals in hydrothermal veins located at the contact between blueschist and eclogite in exhumed rocks in the Tian Shan complex, NW China. These hydrothermal veins were interpreted by Gao et al. (2007) as evidence for local (cm

398 to m) transport of HFSE in aqueous fluid evolved during prograde metamorphic dehydration.
399 The eclogite records conditions of ~1.9 GPA and 500 to 600°C, and the vein records conditions
400 of 1.9 GPa and 490 to 580°C. They reported the presence of aqueous fluid inclusions with
401 salinities of 1.57 to 4.49 wt% NaCl equivalent, and concluded that Nb, Ti and Ta were
402 scavenged by an aqueous fluid during the dehydration of blueschist to eclogite. The new
403 experimental data indicate that Nb would be increasingly mobile in a fluid of this composition.
404 Gao et al. (2007) reported that fluid evolution and migration fractionated Nb, Ti and Ta from Zr
405 and Hf, which were sequestered by titanite. Gao et al. (2007) reported that rutile and apatite co-
406 precipitated in the hydrothermal veins. Precipitation of Cl- and F-bearing apatite would result in
407 rapid depletion of these halogens in the fluid, resulting in destabilization of HFSE-fluorine
408 and/or HFSE-chlorine complexes in the fluid. In turn, this would result in precipitation of rutile,
409 which would deplete the fluid in other HFSE such as Nb owing to the strong partitioning of
410 HFSE into rutile.

411 The sum of observations from natural and experimental systems demonstrate that Nb and
412 other HFSE are in fact mobile in aqueous fluid, and that hydrothermal transport is a function of
413 fluid composition, temperature, and for fluids with ≤ 10 wt% NaCl equivalent, also dependent on
414 pressure and fluid density. However, if rutile is a residual phase, then partitioning of Nb into
415 rutile is favored (i.e., $D_{Nb}^{rutile/fluid} > 1$) over a wide range of pressure and temperature (0.5 to 6.5
416 GPa and 300-1100°C) such that prograde fluid loss during subduction requires very high time-
417 integrated fluid to rock ratios to effectively transfer HFSE from the slab into the mantle wedge.
418 In some arc settings this seems plausible. For example, John et al. (2004) reported that the
419 mineral chemistry of exhumed eclogites in some cases records fluid-rock interaction wherein the
420 total amount of fluid was equivalent to 80% of the total rock mass. In the case of alkaline

421 magma-related ore deposits, such as the world-class Bayan Obo deposit in China, the efficient
422 mass transfer of Nb and other HSFE in alkaline magma to ore fluid may reflect the complete
423 absence of a titanate phase during evolution and migration of a saline hydrothermal fluid.
424

ACKNOWLEDGEMENTS

We acknowledge NSF EAR 1264560 to Simon, Tschauner and Burnley. Portions of this work were performed at HPCAT (Sector 16), Advanced Photon Source (APS), Argonne National Laboratory. HPCAT operations are supported by DOE-NNSA under Award No. DE-NA0001974 and DOE-BES under Award No. DE-FG02-99ER45775, with partial instrumentation funding by NSF. HiPSEC, UNLV, provided HDACs and part of the beamtime. HiPSEC is supported by the National Nuclear Security Administration through DOE Cooperative Agreement #DE-NA0001982. APS is supported by DOE-BES, under Contract No. DE-AC02-06CH11357. We acknowledge COMPRESS and GSECARS for the use of the laser drilling system. *J.M.H. thanks the Canadian Natural Sciences and Research Council (NSERC) for partial support for this research in the form of a Discovery Grant, and Memorial University of Newfoundland, for additional financial support for this project.*

REFERENCES

Abramson, E.H., and Brown, J.M. (2004) Equation of state of water based on speeds of sound measured in the diamond-anvil cell. Geochimica et Cosmochimica Acta, 68, 1827–1835.

Antignano, A., and Manning, C. (2008) Rutile solubility in H_2O, H_2O–SiO_2, and H_2O–$NaAlSi_3O_8$ fluids at 0.7–2.0 GPa and 700–1000 °C: Implications for mobility of nominally insoluble element. Chemical Geology, 255, 283-293.

Audétat, A., and Keppler, H. (2005) Solubility of rutile in subduction zone fluids, as determined by experiments in the hydrothermal diamond anvil cell. Earth and Planetary Science Letters, 232, 393-402.

Bassett, W.A., Shen, A.H., Bucknum, M., and Chou, I.-M. (1993) A new diamond anvil cell for hydrothermal studies to 2.5 GPa and from 190 to 1200 °C. Reviews of Scientific Instruments, 64, 2340-2345.

Bebout, G.E., Ryan, J.G., Leeman, W.P., and Bebout, A.E. (1999) Fractionation of trace elements by subduction zone metamorphism- effect of convergent- margin thermal evolution. Earth and Planetary Science Letters, 171, 63-81.

Bose, K., and Ganguly, J. (1995) Experimental and theoretical studies of the stabilities of talc,

antigorite and phase A at high pressures with applications to subduction processes. Earth and Planetary Science Letters, 136, 109.

Brenan, J.M., Shaw, H.F., Phinney, D.L., and Ryerson, F.J. (1994) Rutile-aqueous fluid partitioning of Nb, Ta, Hf, Zr, U and Th: implications for high field strength element depletions in island-arc basalts. Earth ad Planetary Science Letters, 128, 327-339.

Brophy, J.G., and Marsh, B.D. (1986) On the Origin of High-Alumina Arc Basalt and the Mechanics of Melt Extraction. Journal of Petrology, 27, 763-789.

Brouwer, F.J., Sorensen, S.S., and Philippot, P. (2012) Physical and chemical evolution of subduction-related eclogites: Interplay of inheritance, alteration, deformation and metamorphism. AGU fall meeting abstract, V43C-2861.

Burnley, P.C., and Getting I.C. (2012) Creating a high temperature environment at high pressure in a gas piston cylinder apparatus. Review of Scientific Instruments, 83, 014501.

Dorogokupets, P.I., and Dewaele, A. (2007) Equation of state of MgO, Au, Pt, NaCl-B1 and NaCl-B2: Internally consistent high-temperature pressure scales. High Pressure Research, 27, 431-446.

Foley, S.F., Barth, M.G., and Jenner, G.A. (2000) Rutile/melt partition coefficients for trace elements and an assessment of the influence of rutile on the trace element characteristics of subduction zone magmas. Geochimica et Cosmochimica Acta, 64, 933-938.

Gao, J., John, T. Klemd, R., and Xiong, X. (2007) Mobilization of Ti–Nb–Ta during subduction: Evidence from rutile-bearing dehydration segregations and veins hosted in eclogite, Tianshan, NW China. Geochimica et Cosmochimica Acta, 71, 4974-4996.

Gill J. B. (1981) Orogenic Andesites and Plate Tectonics. Springer- Verlag, 390.

Green T. H. (1981) Experimental evidence for the role of accessory phases in magma genesis.

Journal of Volcanology and Geothermal Research, 10, 405-422.

Hacker, B.R. (2008) H_2O subduction beyond arcs. Geochemistry Geophysics Geosystems, 9, 1-24.

Hammersley, A.P. (1997) FIT2D: An Introduction and Overview. ESRF Internal Report, ESRF97HA02T.

Hanchar, J.M., Finch, R.J., Hoskin, P.W.O, Watson, E.B., Cherniak, D.J., and Mariano, A.N., (2001) Rare earth elements in synthetic zircon: Part 1. Synthesis, and rare earth element and phosphorus doping. American Mineralogist, 86, 667-680.

Hawkesworth C. J., Hergt J. M., Ellam R. M., and Dermott F. M. (1991) Element fluxes associated with subduction related magmatism. Philosophical Transactions of the Royal Society of London, 335, 393–405.

Hawksworth, C.J., Gallagher, K., Hergt, J.M., and McDermott, F. (1993a) Mantle and slab contributions in arc magmas. Annual Review of Earth and Planetary Sciences, 21, 175-204.

Hawkesworth, C.J. (1993b) Trace Element Fractionation Processes in the Generation of Island Arc Basalts. Philosophical Transactions of the Royal Society of London, Series A, 342, 179-191.

Hayden, L.A., and Manning, C.E. (2011) Rutile solubility in supercritical $NaAlSi_3O_8$-H_2O fluids. Chemical Geology, 284, 74-81.

Hernlund, J., Leinenweber, K., Locke, D., and Tyburczy, J.A. (2006) A numerical model for steady-state temperature distributions in solid-medium high-pressure cell assemblies. American Mineralogist, 91, 295-305.

Jenner, G.A., Foley, S.F., Jackson, S.E., Green, T.H., Fryer, B.J., and Longerich, H.P. (1994) Determination of partition coefficients for trace elements in high pressure-temperature

experimental run products by laser ablation microprobe-inductively coupled plasma-mass spectrometry (LAM-ICP-MS). Geochemica et Cosmochimica Acta, 58, 5099-5103.

John, T., Scherer, E., Haase, K., and Schenk, V. (2004). Trace element fractionation during fluid-induced eclogitization in a subducting slab: trace element and Lu-Hf / Sm-Nd isotope systematics. Earth and Planetary Science Letters, 227, 441-456.

Kelemen, P.B., Johnson, K.T.M., Kinzler, R.J., and Irving, A.J. (1990) High-field-strength element depletions in arc basalts due to mantle–magma interaction. Nature, 345, 521-524.

Kerrigan, R.J. (2011) Reaction Rates and textural development of hydrolysis reactions in the system MgO-SiO2-H2O. Dissertation, University of Maryland.

Manning, C.E., Wilke, M., Schmidt, C., and Cauzid, J. (2008) Rutile solubility in albite-H_2O and $Na_2Si_3O_7$-H_2O at high temperatures and pressures by in-situ synchrotron radiation micro-XRF. Earth and Planetary Science Letters, 272, 730-737.

Manning, C. E. (2004) The chemistry of subduction-zone fluids. Earth and Planetary Science Letters, 223, 1-16.

Manning, C. E., and Boettcher, S. L. (1994) Rapid-quench hydrothermal experiments at mantle pressures and temperatures. American Mineralogist, 79, 1153-1158.

Mantegazzi, E. (2013) PVTx properties of saline aqueous fluids at high P-T conditions from acoustic velocity measurements using Brillouin scattering spectroscopy. PhD Dissertation, ETH Zürich.

McCulloch, M.T., and Gamble, J.A. (1991) Geochemical and geodynamical constraints on subduction zone magmatism. Earth and Planetary Science Letters, 102, 358-374.

Morris, J.D., Leeman, W.P., and Tera, F. (1990) The subducted component in island arc lavas: Constraints from Be isotopes and B-Be systematics. Nature, 344, 31-36.

523 Pearson, R.G. (1963) Hard and soft acids and bases. Journal of the American chemical society,
524 85, 3533-3539.
525 Pettke, T. (2006) In situ laser-ablation-ICP-MS chemical analysis of melt inclusion and prospects
526 for constraining subduction zone magmatism. Min. Ass. of Canada Short Course, 36, 51-80.
527 Rapp, J.R., Klemme, S., Butler, I.B., and Harley, S.L. (2010) Extremely high solubility of rutile
528 in chloride and fluoride-bearing metamorphic fluids: An experimental investigation.
529 Geology, 38, 323.
530 Ryerson, F.J. and Watson, E.B. (1987) Rutile saturation in magmas: implications for Ti Nb Ta
531 depletion in island-arc basalts. Earth and Planetary Science Letters, 86, 225-239.
532 Sanchez-Valle, C., Martinez, I., Daniel, I., Philippot, P., Bohic, S., and Simionovici, A. (2003)
533 Dissolution of strontianite at high *P-T* conditions: An in situ synchrotron X-ray fluorescence
534 study. American Mineralogist, 88, 978–985.
535 Saunders A. D., Tarney J., and Weaver S. D. (1980) Transverse geochemical variations across
536 the Antarctic Peninsula: implications for the genesis of calc-alkaline magmas. Earth and
537 Planetary Science Letters, 46, 344–360.
538 Schmidt, C., Rickers, K., Bilderback, D.H., and Huang, R. (2007) In situ synchrotron radiation
539 XRF study of REE phosphate dissolution in aqueous fluids to 800 °C. Lithos, 95, 87-102.
540 Siegbahn, P.E.M. (1993) A comparative study of the bond strengths of the second row transition
541 metal hydrides, fluorides, and chlorides. Theoretica Chimica Acta, 86, 219-228.
542 Singer, D.A. (1986) Grade and tonnage model of carbonatite deposits. *In* Cox, D.P. and Singerl,
543 D.A., eds., Mineral deposit models. United States Geologial Survey Bulletin, 1693, 51.
544 Stalder, R., Foley, S.F., Brey, G.P., and Horn, I. (1998) Mineral-aqueous fluid partitioning of
545 trace elements at 900-1200^{o}C and 3.0-5.7 GPa: New experimental data for garnet,

546 clinopyroxene, and rutile, and implications for mantle metasomatism. Geochimica et
547 Cosmochimica Acta, 62, 1781-1801.
548 Tanis, E.A., Simon, A.C., Tschauner, O. Chow, P., Xiao, Y. Shen, G., Hanchar, J.M., and Frank,
549 M. (2012) Solubility of xenotime in a 2 M HCl aqueous fluid from 1.2 to 2.6 GPa and 300 to
550 500 °C. American Mineralogist, 97, 1708–1713.
551 Timofeev, A., Migdisov, A.A. ,and Williams-Jones, A.E. (2014) The solubility and speciation of
552 niobium in fluoride-bearing aqueous solutions. Goldschmidt Conference.
553 Tropper, P., and Manning, C.E. (2005) Very low solubility of rutile in H_2O at high pressure and
554 temperature, and its implications for Ti mobility in subduction zones. American
555 Mineralogist, 90 (2-3), 502-50.
556 Verplanck, P.L., and van Gosen, B.S. (2011) Carbonatite and alkaline intrusion-related rare earth
557 element deposits – A deposit model. United States Geological Survey Open File Report,
558 1256.
559 Wojdyr, M. (2010) Fityk: a general-purpose peak fitting program. Journal of Applied
560 Crystallography, 43, 1126–1128.
561 Woodhead, J., Eggins, S., and Gamble, J. (1993) High field strength and transition element
562 systematics in island arc and back-arc basin basalts: evidences for multi-phase melt
563 extraction and a depleted mantle wedge. Earth and Planetary Science Letters, 114, 491-504.

564 FIGURE CAPTIONS

565 Figure 1: The experimental P-T conditions for the current study are plotted with respect to
566 subduction paths for cold and hot subduction (cf. Hacker et al., 2008). The P-T conditions for
567 published experimental data for the solubility of pure rutile in H_2O (circles, Tropper and
568 Manning, 2005; Audétat and Keppler, 2005; Antignano and Manning 2008; Rapp et al., 2010),
569 NaCl- (triangles, Rapp et al., 2010) and NaF- (diamonds, Rapp et al., 2010) bearing aqueous
570 fluids. The P-T conditions of studies of Nb partitioning between rutile and aqueous fluid and
571 silicate melt are also plotted (pentagons, Brenan et al., 1994, Stalder et al., 1998, Foley et al.,
572 2000).

573

574 Figure 2: EPMA-determined Nb (squares) and Mo (triangles) concentrations (wt%) of randomly
575 selected starting crystals as a function of distance from the rim towards the center of the crystal
576 (a, b, c), and LA-ICP-MS depth profiles through the crystals (d, e).

577

578 Figure 3 a-b: The LA-ICP-MS depth profiles of ^{49}Ti (blue circles) and ^{93}Nb (red squares)
579 concentrations in the (a) starting crystal and run-product crystal from the piston cylinder-mass
580 experiment 2013_03_14. Gas background is measured for the first 30-40 seconds at which time
581 the laser is turned on and used to ablate into the crystal.

582

583 Figure 4 a-c: a) (top left) and b) (top right) 2-D and 3-D, respectively, false-color maps of x-ray
584 beam intensity that passed through sample chamber: c) (bottom left) and d) (bottom right) 2-D
585 and 3-D false-color maps, respectively, of the Nb signal intensity from the sample chamber. The
586 color bar is based on beam (for a and b) or Nb intensity (for c and d). Red colors are high

intensity and purple colors are low intensity. The scale is divided into 4000 count increments for beam intensity and 10 count increments for Nb intensity.

Figure 5 a-b: Date from the current study and published (Foley et al., 2000; Brenan et al., 1994, Stalder et al., 1998) for Nb concentrations in experimental aqueous fluids plotted as a function of a) temperature, b) pressure, and c) fluid density. Uncertainties for Nb (ppm) are discussed in the text.

595
596 Table 1: HDAC-SXRF experimental conditions and results

Experiment[a]	Fluid Type (wt%)	Temperature (°C)	Pressure (GPa) ($\pm 1\sigma$)	Fluid Density (g/cm^3)	ppm Nb in the fluid ($\pm 1\sigma$)
20110801	10% NaCl	300	2.10(0.1)	1.25	7.3(1.4)
20110801	10% NaCl	400	2.80(0.1)	1.28	9.4(1.2)
20110801	10% NaCl	500	2.80(0.1)	1.25	13.4(2)
20110804	20% NaCl	300	2.05(0.1)	1.38	191(31)
20110804	20% NaCl	400	2.62(0.1)	1.41	215(29)
20110804	20% NaCl	500	4.56(0.2)	1.54	233(29)
20110804	20% NaCl	600	6.36(0.2)	1.63	233(36)
20110805	20% NaCl	300	1.80(0.1)	1.21	86(8)
20110805	20% NaCl	400	2.60(0.1)	1.27	86(9)
20110805	20% NaCl	500	4.50(0.2)	1.38	74(10)
20120802	4% NaF	308	5.14(1.1)	1.48	285(37)
20120802	4% NaF	401	5.19(1.1)	1.46	831(95)
20120802	4% NaF	503	6.53(1.4)	1.49	1073(106)
20130202	4% NaF	300	3.21(0.4)	1.35	333(124)
20130202	4% NaF	400	3.48(1.0)	1.32	426(42)
20130205	4% NaF	300	2.13(0.6)	1.25	272(28)
20130205	4% NaF	400	2.48(0.3)	1.25	1226(176)
20130205	4% NaF	500	3.07(0.4)	1.27	1339(99)

597 [a]Each experimental SXRF run allows us to measure the concentration of Nb in aqueous fluid at
598 multiple P-T conditions.
599

600 Table 2: Piston cylinder experimental conditions and results

Experiment ID	20130314	20130522	20130527[b]
Fluid Composition (wt%)	10% NaCl	10% NaCl	4% NaF
Time (h)	8:31	27:15:00	12:00
Temperature (^{o}C) ($\pm1\sigma$)	687(2)	793(11)	692(7)
Pressure (GPa) ($\pm1\sigma$)	1.09(0.06)	1.04(0.02)	0.97(0.02)
Fluid (mg)	23.4	31.2	29.5
Fluid Density (g/cm^3)	1.06	1.01	0.91
[a]Crystal weight in (µg) ($\pm1\sigma$)	547(12)	887 (5)	1088 (1)
[a]Crystal weight out (µg) ($\pm1\sigma$)	523(6)	734 (5)	813 (162)
Mass loss (µg)	24	153	275
[c]Wt% Nb in product crystal	0.9307(.04)	1.0456(0.06)	1.0275(0.22)
[d]ppm Nb in Fluid (error)	35(34)	250(179)	650(400)

601

602 [a]The crystal was weighed four times to ensure accurate weight and the average is presented. The
603 standard deviation of the average weight is provided in the parentheses.
604 [b]Run products contained broken crystal fragments as well as the primary crystals.
605 [c]Wt% Nb for final run products are from LA-ICP-MS analysis.
606 [d]Error is calculated by propagating the error from weighing, the analytical error from the LA-
607 ICP-MS, and the *possible* 5wt% rim.

608 FIGURES

609 Figure 1

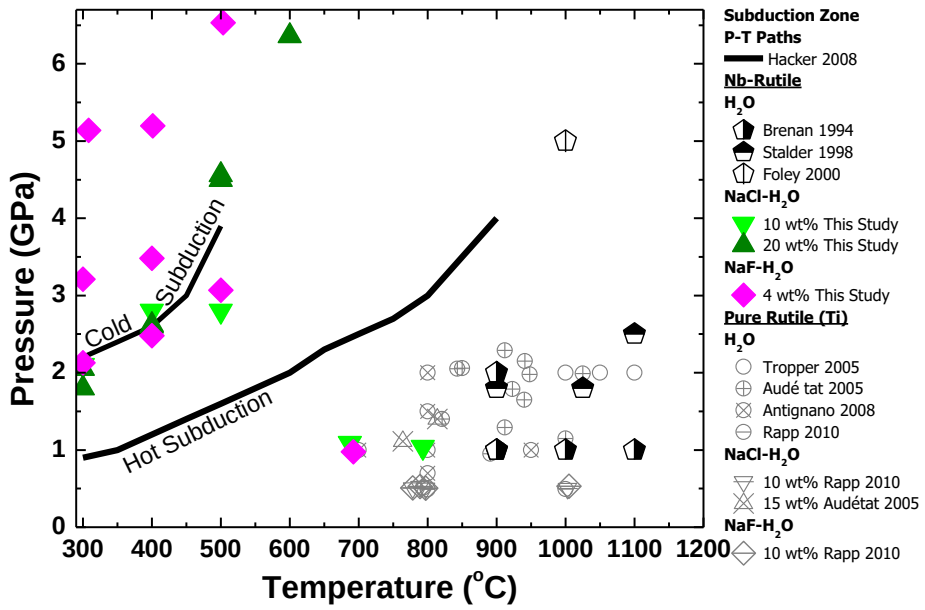

610

611 Figure 2

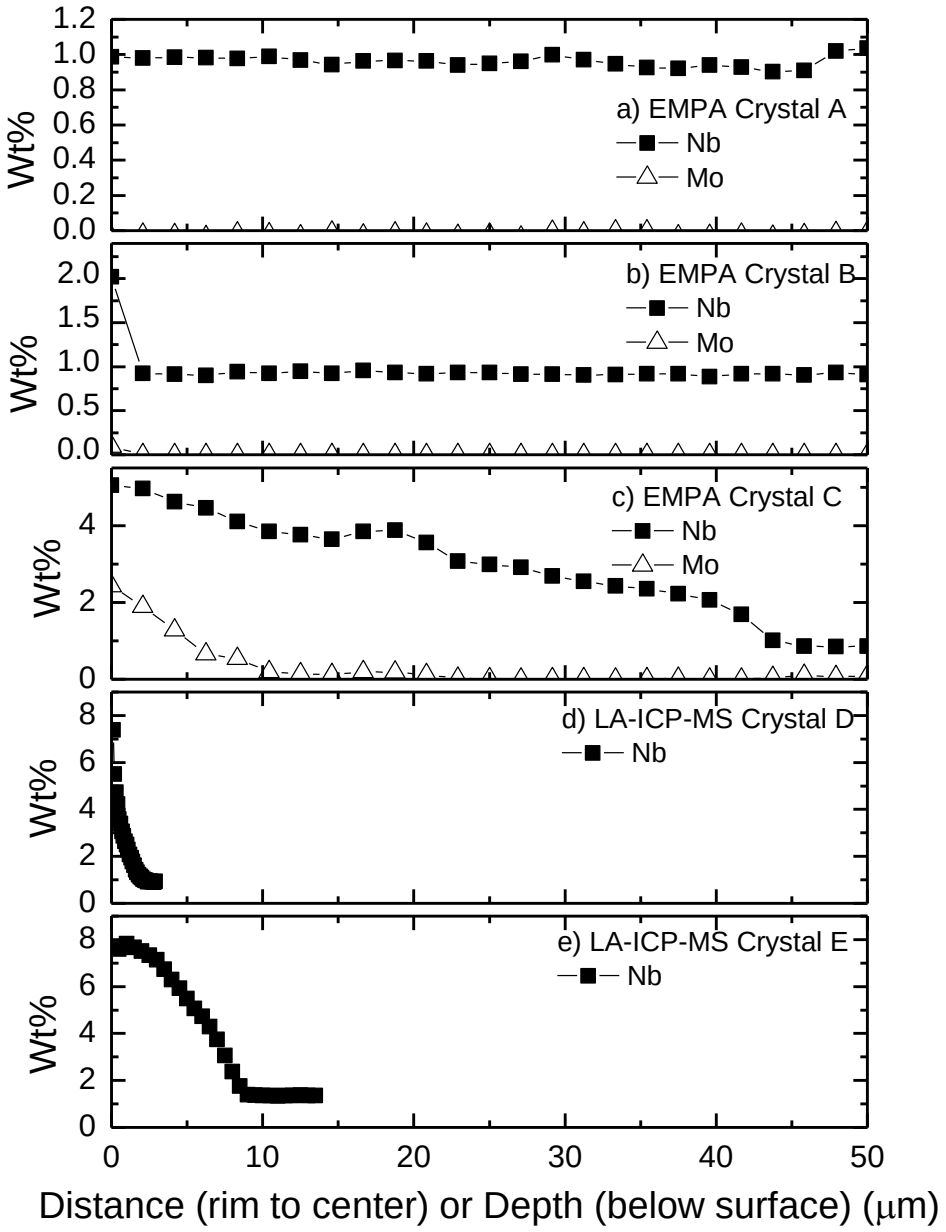

612

613 Figure 3

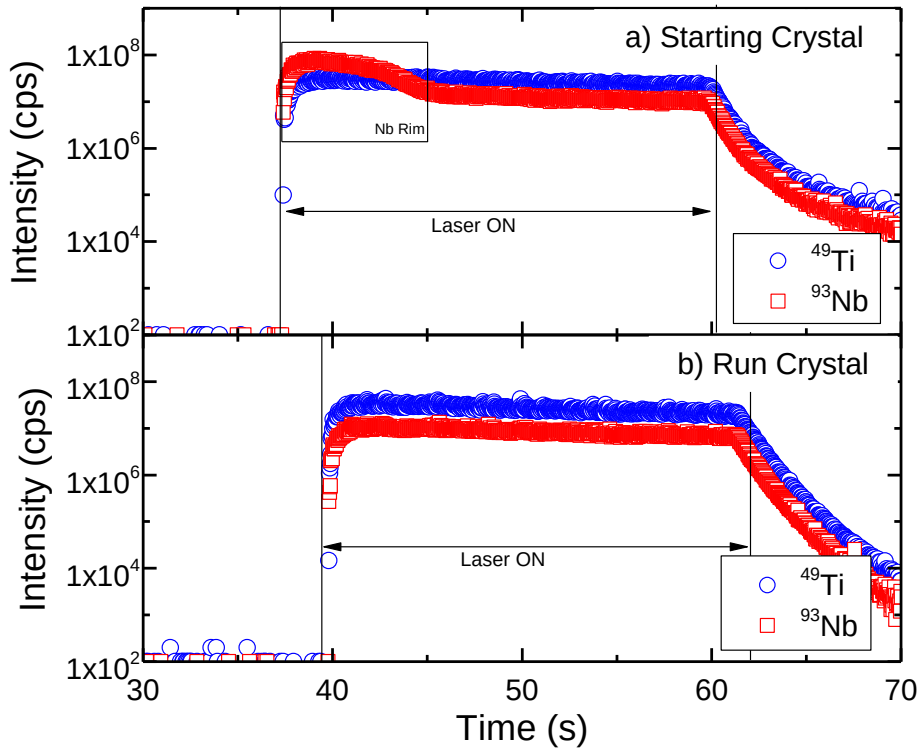

614

615

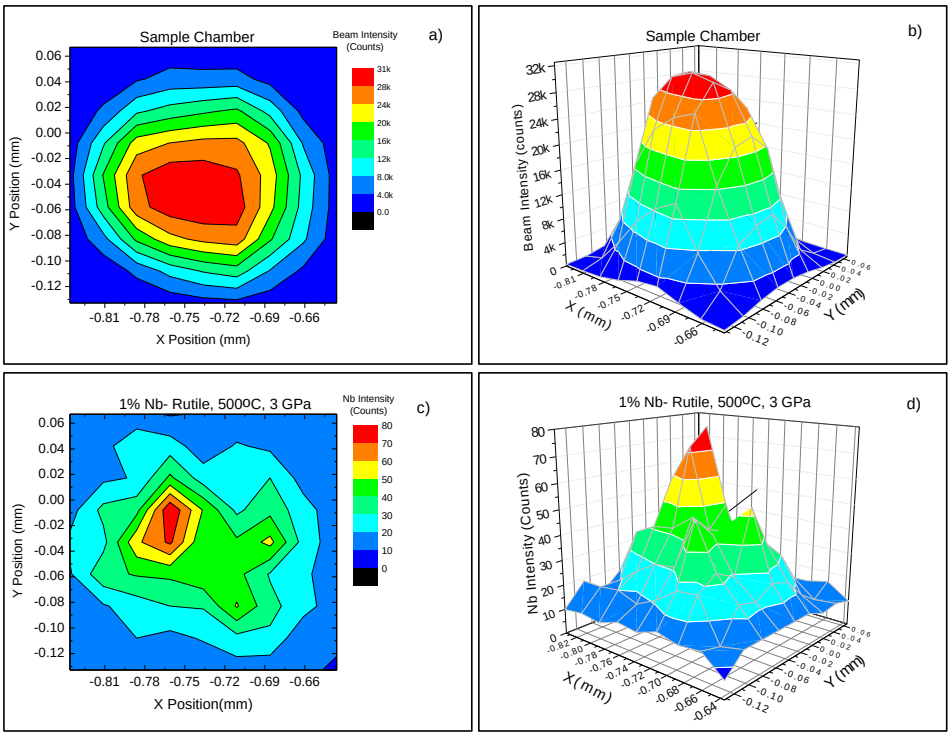

616

617 Figure 4

618 Figure 5:

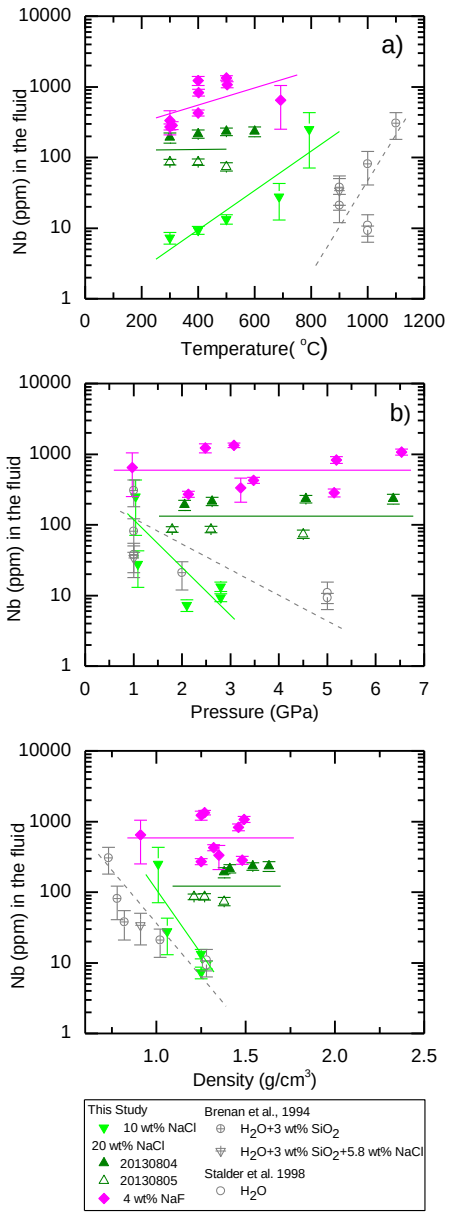

619